IET Generation, Transmission & Distribution

ORIGINAL RESEARCH

Implementation and laboratory verification of method utilizing phase and neutral quantities for detection and location of low-current earth faults in resonant grounded networks

Thomas Treider [ORCID] | **Hans Kristian Høidalen**

Department of Electric Energy, Norwegian University of Science and Technology, Trondheim, Norway

Correspondence

Thomas Treider, Department of Electric Energy, Norwegian University of Science and Technology, Trondheim, Norway.
Email: thomas.treider@ntnu.no

Abstract

Earth faults is a challenging fault type to locate in resonant grounded networks due to their naturally low fault current, and the problem increases with an increased fault impedance. This paper describes the detailed implementation and laboratory testing of a method for detection, location and clearing of earth faults with very small fault currents. The method consists of two indicators used in the fault detection stage, where their simultaneous operation ensures selective fault detection and faulty feeder selection. One of these indicators also enables continuous fault indication throughout a sectionalizing process. The laboratory tests demonstrate that both indicators function as intended, and it is the current sensors which ultimately limit the attainable sensitivity. Faults up to 15 kΩ were detected successfully in the laboratory network based on phase current measurements, while the sectionalizing indicator showed much higher sensitivity and functioned as intended in a 50 kΩ fault. Measurements from one field test in a 22 kV network corroborate the laboratory results and demonstrate the expected earth fault indicator response.

1 | INTRODUCTION

Earth faults in resonant grounded systems represent a particularly challenging case for protection systems due to their very low fault currents. As a result, conventional protection systems such as over-current and distance protection can not be used. Large fault impedances also create problems for transient based earth fault protection due to the absence of earth fault transients with sufficient magnitude. The terms "high impedance" and "low current" are relative terms, given different meaning by different authors in the scientific literature. While for example Norwegian regulations require detection of faults up to 3 kΩ [1], faults up to hundreds of kΩ's are not uncommon [2, 3]. High impedance faults may evolve into more serious faults over time, so it is of interest to be able to detect them as early as possible. Therefore, this paper is concerned with faults above 3 kΩ.

Specialized earth fault location schemes have been proposed extensively in the literature. The magnitude of the neutral voltage is the standard fault detecting approach in the case of low impedance faults, but this is not reliable in the case of very high fault impedances [3]. The neutral voltage increment can be used instead to provide sensitive detection [3], while the slow transient build-up of the fault current is used in [4]. The method presented in [5] uses the deviation of the neutral voltage and current from their known healthy values to estimate an equivalent fault resistance, and a sufficiently low resistance estimate signifies a fault. Methods based on the admittance-principle are also common, monitoring the ratio of the zero-sequence voltage and current to obtain detection and directionality [6].

Fault location may be implemented as a separate stage or integrated with the fault detection stage. If not integrated with the fault detection, it can then be either passive or active. Active methods can for instance involve injection of a super-imposed signal that can be traced in the network [7, 8], or a short-time de-tuning of the arc suppression coil (ASC) [5, 9, 10]. The drawbacks of such methods are the added complexity and the need for external equipment or integration with the ASC controller. Reference [11] describes a mobile solution based on injection of non-fundamental frequency currents. This is however meant for ground personnel and represents a much slower, manual localization process. Decentralized or wide-area methods using either fault passage indicators (FPIs) [6] or feeder terminal units

(FTUs) [12] have also been proposed, requiring more units and infrastructure to provide sufficient coverage.

Several passive methods for earth fault location can also be found in the literature. In [13] it is proposed to monitor the zero-sequence energy on each feeder, where the sign of the energy will indicate forward/reverse fault. The authors of [14] report that this principle becomes less reliable for very high fault impedances combined with network asymmetry, and [15] further illustrates the problem with asymmetry. In [16], very sensitive detection is achieved based on a charge similarity approach. However, the method assumed and was verified with a perfectly symmetrical network in which no zero-sequence currents flow in healthy operation. Real networks can have considerable asymmetry [17] in which the high impedance fault may be difficult to separate from the natural asymmetry, and it may even temporarily reduce the asymmetry [3]. Reference [18] proposes a complex method where the faults are detected based on neutral voltage displacement, the faulty phase is identified based on the phase voltage variations, and a transient principle is applied to locate the faulty feeder. Again, the asymmetry of the network is mentioned as a limitation, and the method requires several relay units in the network for faulty section determination.

To deal with the problem of measurement errors and network asymmetry, current and voltage increments are often used [3, 19–21]. This enables more sensitive detection as the healthy state asymmetry contribution can be canceled out. These methods generally report very sensitivity, that is, in the 10-200 kΩ range.

Except for reference [5], it is only the task of fault detection and an initial faulty feeder indication which is emphasized in the literature, whereas the ability to provide continuous fault indication throughout a sectionalizing process is neglected. In [5] the fault indication is achieved using a short-time de-tuning of the ASC to map the parameters of the healthy system, but it is not apparent how reliable this is during sectionalizing. Fault indication during a sectionalizing process is an important feature to consider as (1) the initial faulty feeder indication may be inconclusive or wrong, and (2) it may be of interest to determine the faulted section more precisely, not just the faulted feeder. High impedance faults are not time critical, and it is preferable to isolate the faulty part of the network systematically while affecting a limited number of customers. During this process fault indication based on the increments of the feeder currents will be inaccurate, and the neutral voltage magnitude, which can serve this purpose during low-impedance faults, is not reliable when the fault impedance is very high due to its much lower displacement during fault and its possibly equally large displacement during sectionalizing.

This paper contributes with the following: First, the detailed implementation of a novel method for detection and location of earth faults with very low fault currents in compensated networks. The method is based on two independent fault current estimates which together provide sensitive and selective fault detection. One of these estimates is based on the phase currents on each feeder, while the other makes use of the ASC current, voltage and compensation degree. The method also enables continuous monitoring of the fault's presence in the network
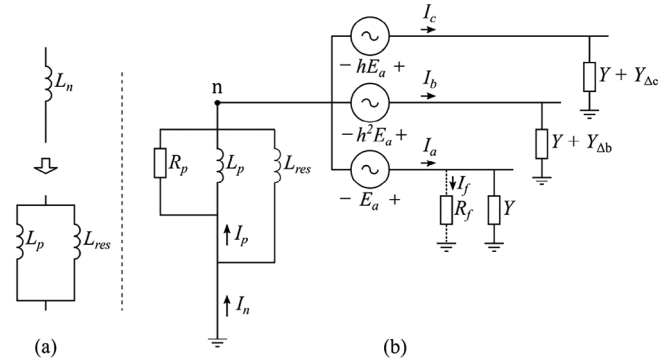

FIGURE 1 (a) Neutral point impedance coil split and (b) network model.

during sectionalizing, and it can therefore aid operators when clearing the fault. Second, this paper presents laboratory tests to validate the proposed method, and to investigate factors limiting the sensitivity. A physical 400 V laboratory network model is used for this purpose, which enables real-life complicating factors such as measurement sensor accuracy and off-nominal network frequency to be included in the tests. The paper also discusses the applicability of such laboratory tests as substitutes for field tests.

The rest of the paper is organized as follows: Section 2 describes the theoretical foundation for the method, and this is used to derive the proposed fault detection and location method which is presented in Section 3. Section 4 describes the laboratory test setup, and the results from these tests are presented in Section 5. The applicability of the results is discussed along with the challenge of transferring the laboratory results to a real network in Section 6, and conclusions are given in Section 7.

2 | MODELLING EARTH FAULTS

The theoretical foundation for the method discussed in this paper has previously been published in shorter format in reference [22], but it is included here for the sake of readability and further development.

2.1 | Neutral coil split

Consider a network compensated by an ASC tuned to some degree $k > 0$, so that its value L_n is given by (1).

$$L_n = \frac{1}{k} \cdot L_{res}. \tag{1}$$

The inductance L_{res} corresponds to the resonance condition, that is, the coil inductance which compensates for the total shunt capacitance of the network C_{tot} as described by (2).

$$\frac{1}{j\omega L_{res}} + j\omega C_{tot} = 0. \tag{2}$$

The coil L_n is replaced, in theory, by two coils in parallel, L_{res} and L_p, such that $L_n = L_{res} || L_p$. This is illustrated in Figure 1a. The coil L_p is related to the actual value of the physical coil L_n

through the compensation degree k as described by (3).

$$L_p = \frac{k}{k-1} \cdot L_n.$$ (3)

The benefit of introducing this notation is the more compact form of the equations derived in this paper as the total capacitance to ground in the system is cancelled by L_{res}, as described in (2).

2.2 | Neutral voltage

In the network in Figure 1b the total phase-ground admittances for the three phases are as given in (4),

$$
\begin{aligned}
Y_a &= Y = G + j\omega C, \\
Y_b &= Y + Y_{\Delta b} = G + G_{\Delta b} + j\omega(C + C_{\Delta b}), \\
Y_c &= Y + Y_{\Delta c} = G + G_{\Delta c} + j\omega(C + C_{\Delta c}),
\end{aligned}
$$ (4)

where C and G are the total phase-ground capacitance and conductance in phase a, respectively, and $C_{\Delta b}, C_{\Delta c}, G_{\Delta b}$ and $G_{\Delta c}$ describe the deviation of capacitance and conductance in phases b and c with respect to phase a that stems from the natural asymmetry in the network. The neutral voltage in the healthy network can be expressed as

$$\vec{V}_n = -\vec{E}_a \frac{D}{\hat{G} + \frac{1}{R_p} + \frac{1}{j\omega L_p}},$$ (5)

where $\vec{E}_a$ is the phase-neutral voltage of the reference phase, in this case phase a, and

$$
\begin{aligned}
D &= h^2 Y_{\Delta b} + h Y_{\Delta c}, \\
\hat{G} &= 3G + G_{\Delta b} + G_{\Delta c}.
\end{aligned}
$$ (6)

In (6), the operator $h = e^{j120°}$. The resistor R_p represents the coil losses as well as any external resistor which may be permanently connected. When a fault occurs in phase a, the neutral voltage becomes instead as given in (7).

$$\vec{V}_n = -\vec{E}_a \frac{D + \frac{1}{R_f}}{\hat{G} + \frac{1}{R_f} + \frac{1}{R_p} + \frac{1}{j\omega L_p}}.$$ (7)

2.3 | Fault current

Assuming a fault taking place in phase a, the fault current according to Figure 1 is
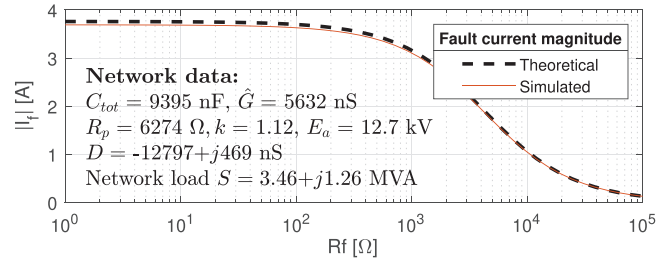
$$\vec{I}_f = \frac{\vec{V}_n + \vec{E}_a}{R_f}.$$ (8)

FIGURE 2 Fault current magnitude estimated using (9) and simulations in ATP.

Network data:
$C_{tot} = 9395$ nF, $\hat{G} = 5632$ nS
$R_p = 6274\ \Omega, k = 1.12, E_a = 12.7$ kV
$D = -12797 + j469$ nS
Network load $S = 3.46 + j1.26$ MVA

A more useful expression for the fault current in the system can be derived by combining (7) and (8):

$$\vec{I}_f = \vec{E}_a \frac{1}{R_f}\left(\frac{\hat{G} + \frac{1}{j\omega L_p} + \frac{1}{R_p} - D}{\hat{G} + \frac{1}{j\omega L_p} + \frac{1}{R_p} + \frac{1}{R_f}}\right).$$ (9)

Figure 2 shows the magnitude of the fault current as a function of fault resistance for a selected set of network parameters, both from simulations in ATP and by using (9).

3 | METHOD FOR FAULT DETECTION AND LOCATION

3.1 | Estimating the fault current during fault

The fault detection and location method described in this paper relies on two separate approaches for estimating the earth fault current, and the theoretical foundation for both these approaches is explained in the following two subsections of the paper.

3.1.1 | Using the neutral current

Assume that the compensation degree k of the network is known. Then, the current $\vec{I}_p$ flowing through R_p and L_p as illustrated in Figure 1 can be computed based on the measured neutral current $\vec{I}_n$ and voltage $\vec{V}_n$ as shown in (10).

$$\vec{I}_p = \vec{I}_n + \frac{\vec{V}_n}{j\omega L_{res}}.$$ (10)

It can be shown that $\vec{I}_p$ will, during healthy (pre) and faulty (fault) conditions, satisfy (11).

$$
\begin{aligned}
\vec{I}_{p,pre} &= \hat{G}\vec{V}_{n,pre} + D\vec{E}_a, \\
\vec{I}_{p,fault} &= \left(\hat{G} + \frac{1}{R_f}\right)\vec{V}_{n,fault} + \left(D + \frac{1}{R_f}\right)\vec{E}_a.
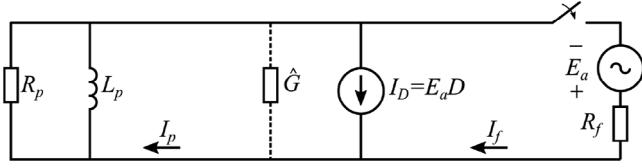\end{aligned}
$$ (11)

FIGURE 3 Equivalent circuit for healthy and faulty network considering the asymmetry as a current source.

By assuming that the voltage $\vec{E}_a$ remains unchanged during the fault, as is reasonable considering small fault currents, and recognizing that the asymmetry factor D is constant as long as the network topology does not change, (12) is obtained. The term $\hat{G}\Delta\vec{V}_n$ is assumed negligible, and thus the fault current can be approximated as $\Delta\vec{I}_p$.

$$\Delta\vec{I}_p = \vec{I}_{p,fault} - \vec{I}_{p,pre} = \hat{G}\Delta\vec{V}_n + \vec{I}_f \approx \vec{I}_f. \quad (12)$$

Equation (12) can also be derived considering Figure 3, which is derived from Figure 1 using Thevenin–Norton transformations. It shows that the current flowing in L_p and R_p in the healthy state is caused by the asymmetry of the system, and if the conductance is assumed negligible, then the current $\vec{I}_{p,pre} = \vec{I}_D = \vec{E}_a D$. When the fault occurs, the switch is closed and the fault current is found as $\vec{I}_f = \vec{I}_p - I_D = \Delta\vec{I}_p$, which is the same result as in (12).

3.1.2 | Using phase currents

The currents flowing onto the feeders are assumed to consist of a load current, a capacitive current to ground, a capacitive current to the two others phases, as well as an induced current caused by the mutual inductance between the phases. Equation (13) shows these components for the healthy state current in phase a.

$$\vec{I}_a = (\vec{V}_n + \vec{E}_a)Y + \vec{V}_{ab}j\omega C_{ab} + \vec{V}_{ac}j\omega C_{ac} + \vec{I}_{ind.} + \vec{I}_{load}. \quad (13)$$

When a fault occurs in the network in Figure 1, the phase currents will change. By assuming that (1) line voltages remain constant during fault, (2) the loads remain unchanged due to the constant line voltages, and (3) that the change in phase current magnitude is so small that the induced currents can be assumed constant, then (14) describes the changes in phase currents during a fault in phase a.

$$\Delta\vec{I}_a = \Delta\vec{V}_n Y + \vec{I}_f,$$

$$\Delta\vec{I}_b = \Delta\vec{V}_n(Y + Y_{\Delta b}), \quad (14)$$

$$\Delta\vec{I}_c = \Delta\vec{V}_n(Y + Y_{\Delta c}).$$

These current increments can be combined to produce three earth-fault indicators, named J_a, J_b and J_c, as described by (15).

$$J_a = \Delta\vec{I}_a - \frac{1}{2}(\Delta\vec{I}_b + \Delta\vec{I}_c),$$

$$J_b = \Delta\vec{I}_b - \frac{1}{2}(\Delta\vec{I}_a + \Delta\vec{I}_c),$$

$$J_c = \Delta\vec{I}_c - \frac{1}{2}(\Delta\vec{I}_a + \Delta\vec{I}_b). \quad (15)$$

By inserting (14) in (15), and by assuming that $Y_{\Delta b} = Y_{\Delta c} \approx 0$, it is seen that the three earth-fault indicators remain at approximately zero during healthy operation. For an earth-fault in phase a, the three earth-fault indicators on the faulty feeder takes on the values in (16), whereas they remain zero on the healthy feeders.

$$J_{a,fault} = \vec{I}_f, \qquad J_{b,fault} = J_{c,fault} = -\frac{1}{2}\vec{I}_f. \quad (16)$$

As mentioned earlier, the asymmetries $Y_{\Delta b}$ and $Y_{\Delta c}$ can not be assumed to be zero in real networks. Generally, the transition from (15) to (16) becomes less accurate as $Y_{\Delta b}$ and $Y_{\Delta c}$ increase. Equation (17) shows the values of the indicators J_{a-c} during fault when the asymmetries are included:

$$J_{a,fault} = \vec{I}_f - \Delta\vec{V}_n\frac{1}{2}(Y_{\Delta b} + Y_{\Delta c}),$$

$$J_{b,fault} = -\frac{1}{2}\vec{I}_f + \Delta\vec{V}_n\left(Y_{\Delta b} - \frac{1}{2}Y_{\Delta c}\right), \quad (17)$$

$$J_{c,fault} = -\frac{1}{2}\vec{I}_f + \Delta\vec{V}_n\left(-\frac{1}{2}Y_{\Delta b} + Y_{\Delta c}\right).$$

The errors introduced by the asymmetry are only a few percent of the magnitude of the fault current even in the case of very unsymmetrical networks ($D \approx 5\%$ of $3Y$ [17]), and this can be shown to be independent of the fault resistance. As a result, (16) is a valid simplification of (17).

3.2 | Criterion for fault detection

To detect earth faults in the network, it is proposed to monitor the three indicators in (15) on each feeder. During an earth fault they are expected to have a fixed relationship between them as indicated by (16):

1) The magnitude of the faulty phase indicator is approximately twice as large as the magnitudes of the indicators in the two healthy phases.
2) The phase angles of the healthy phase indicators are equal and approximately 180 degrees out of phase with the faulty phase indicator.

For all other fault types, this relationship will not be observed. Asymmetric load changes could in theory result in a similar response from the indicators, but the current $\Delta\vec{I}_p$ is unaffected by load changes and can be used to give an extra criterion for secure detection of earth faults. If the compensation degree of the network is known with reasonable accuracy, the value obtained for $\Delta\vec{I}_p$ should be comparable with the faulty phase indicator, both in magnitude and angle. A similar approach was suggested in [5], although by utilizing zero sequence currents increments on every feeder. The difference is that the

zero sequence currents are less suited to provide information on faulted phase, and directionality can not be obtained without comparing the current increments on all the feeders. The phase current indicators in (15) can perform the required computations without input from the other feeders.

3.3 | Searching for and clearing faults

As the load in the network can not be assumed constant over long periods, the indicators in (15) are not reliable for prolonged fault indication. Once a permanent fault has been detected in the network, the continued monitoring of the fault is done through $\Delta \vec{I}_p$. The pre-fault value $\vec{I}_{p,pre}$ is then no longer updated but instead kept at its last value before the fault was detected. This way $\Delta \vec{I}_p$ remains high as long as the fault is present in the network, whereas it returns to zero if the fault is cleared.

Once the sectionalizing process begins, the ASC is assumed to be kept constant. If a section of the network is disconnected during this process, the compensation degree k increases due to the reduced network capacitance. This increases the value of L_{res}, and the computation of the current $\vec{I}_p$ using (10) must then be done with an updated value of L_{res}. Keeping the current $\vec{I}_{p,pre}$ as an estimate of the current $\vec{I}_D$ in the network is a simplification because the sectionalizing process may alter the asymmetry parameter D, and as a result, the current $\Delta \vec{I}_p$ will most likely not return exactly to zero when the fault is cleared. If the fault current was in the same order of magnitude as this residual value the success of the fault clearing is not possible to determine.

3.4 | Logic implementation and settings

The computation of the current increments is implemented using a sliding window. The current phasors are updated every sample, and the increment of current $\vec{I}$ at sample j is then computed as

$$\Delta \vec{I}_{[j]} = \vec{I}_{[j]} - \vec{I}_{[j-T_{SW} \cdot f_s]}, \quad (18)$$

where T_{SW} is the length of the sliding window in seconds and f_s the sampling frequency in Hz. Based on (16), a fault in phase a can be signaled when the criteria in (19) are met.

$$|\angle J_b - \angle J_a| \in [180° - \phi, 180° + \phi]$$

$$|\angle J_c - \angle J_a| \in [180° - \phi, 180° + \phi]$$

$$\frac{|J_b|}{|J_a|} \in [0.5 - K, 0.5 + K] \quad (19)$$

$$\frac{|J_c|}{|J_a|} \in [0.5 - K, 0.5 + K].$$

The criteria in (19) are visualized in Figure 4, where a fault in phase a is considered. The parameters K and ϕ are margins added to allow for some deviation from the ideal vector relationship in (16). A fault is detected when both the vectors J_b/J_a and J_c/J_a come into the shaded area. Similar zones are imple-
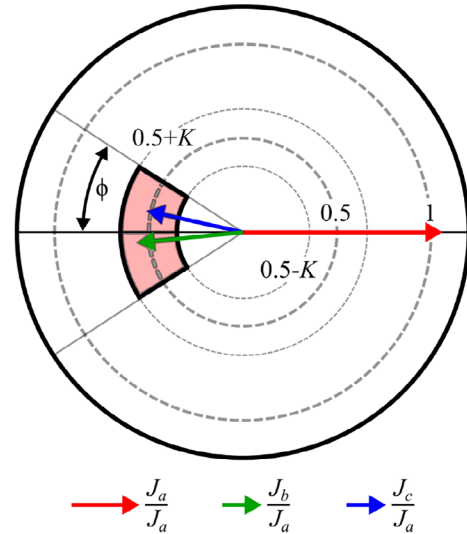

FIGURE 4 Indicator relationship during fault in phase a, with the red field representing "trip zone" for a fault in phase a according to (19).

mented for the fault indication in phases b and c as well, and they are mutually exclusive.

The criteria in (19) are derived from the expected relationship between the vectors J_{a-c}, and in simulations these are sufficient. However, in a physical implementation the indicators are never truly zero. Small fluctuations due to noise and cross-talk from surrounding conductors can cause the criteria in (19) to be met accidentally and quite frequently unless a magnitude threshold is considered. The criterion in (20) is added to account for this.

$$|\vec{J}_a| > \epsilon_J. \quad (20)$$

Adding the magnitude threshold is necessary for secure operation of the indicators, but it does necessarily reduce the sensitivity of the fault detection. Determining the value of this threshold is also a challenge as it must be set higher than the aforementioned noise in healthy operation, and this will require study on the network in question. A final criterion is as mentioned previously to consider the neutral current component $\Delta \vec{I}_p$ as well, discarding all trips from the indicators that do not coincide with a similar response in this current. This way, the neutral current criterion provides added security against false fault detection. The parameter $\Delta \vec{I}_p$ is computed in the same way as the phase current increments, as shown in (18), but with a longer sliding window length T_{SWp} to account for the slower current dynamics in the coil.

A vector comparison between $\Delta \vec{I}_p$ and the faulty phase indicator could be made as well, but this assumes knowledge of the compensation degree k. If k is considered to be uncertain, a simple magnitude criterion like the one in (21) could be used to monitor $\Delta \vec{I}_p$.

$$|\Delta \vec{I}_p| > \epsilon_p. \quad (21)$$

If k is known, (21) is extended to (22) to include a vector comparison such as the one used for the phase current
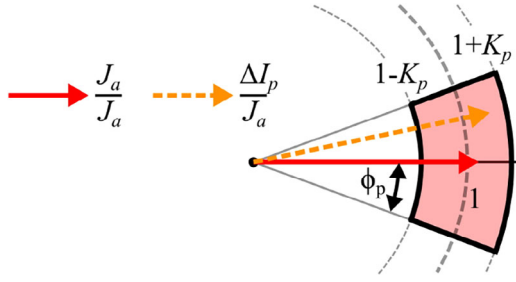
FIGURE 5 Indicator relationship during fault in phase a, with the red field representing "trip zone" for a fault in phase a according to (22).

indicators, where K_p and ϕ_p are margins similar to K and ϕ in (19). Both J_a and $\Delta \vec{I}_p$ should be identical during fault according to (12) and (16), and the detection logic in (22) can be used in addition to (21). Figure 5 illustrates this vector comparison.

$$\frac{|\Delta \vec{I}_p|}{|J_a|} \in [1 - K_p, 1 + K_p] \tag{22}$$

$$|\angle \Delta \vec{I}_p - \angle \vec{J}_a| < \phi_p.$$

Correct values for the settings in (19)-(22) will primarily be affected by the quality of the measurements, and selecting the correct settings to balance the need for precision and avoiding misoperation is the major challenge. Generally, the sliding window length T_{SW} should be long enough to capture the transients during earth faults, but not so long that the load current can not be assumed constant on the interval, making the transition from (13) to (14) incorrect. The window T_{SWp} should be long enough to allow for the current to increase in the coil, but limiting this window length is not critical as the neutral current is relatively constant.

Once a fault has been detected, the computation of $\Delta \vec{I}_p$ using the sliding window is stopped. Assuming that a fault was detected at time t_f, $\Delta \vec{I}_p(t)$ is computed as $\Delta \vec{I}_p(t) = \Delta \vec{I}_p(t) - \Delta \vec{I}_p(t_f - T_{SWp})$ going forward. This way, continuous fault indication is obtained for the sectionalizing process. The phase current indicators can not assist in the sectionalizing process because (1) the load currents can not be assumed constant over many seconds, and (2) the sectionalizing process will necessarily change the phase currents and render (14) invalid. However, their continued calculation using sliding windows is still of interest as the relationship between the indicators that signal a fault is also observed if a fault disappears on its own.

The flowchart in Figure 6 details the fault detection and localization process described above.

4 | TEST SETUP AND MEASUREMENT PROCESSING

4.1 | Norwegian national smart grid laboratory

The laboratory verification is conducted in the distribution network model implemented in the National Smart Grid Lab-
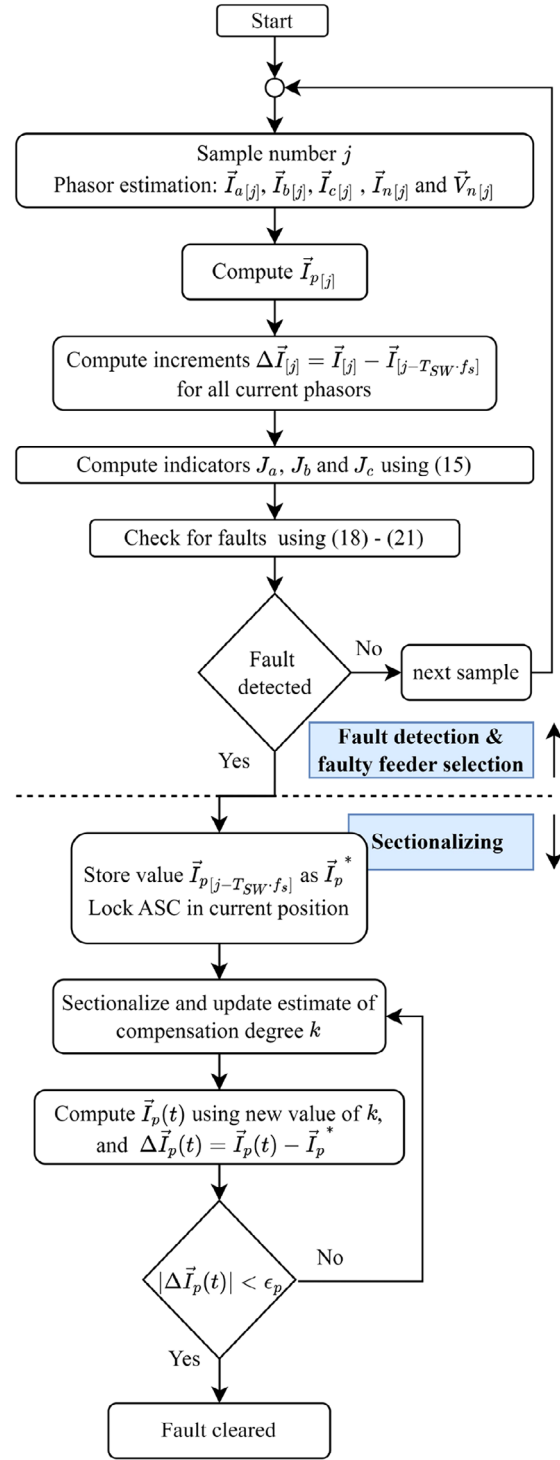

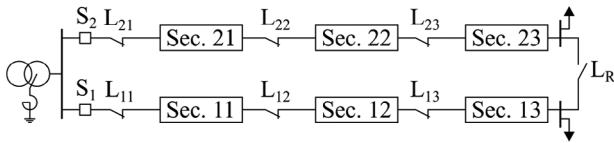**FIGURE 6** Flowchart for fault detection process.

oratory, which is a joint NTNU-SINTEF facility intended for testing of various smart grid technologies [23, 24].

4.1.1 | Distribution network model

The laboratory contains a 400 V distribution network model which is constructed using physical resistors, inductances and capacitors to emulate a real distribution network. Figure 7

TABLE 1   Laboratory equipment.

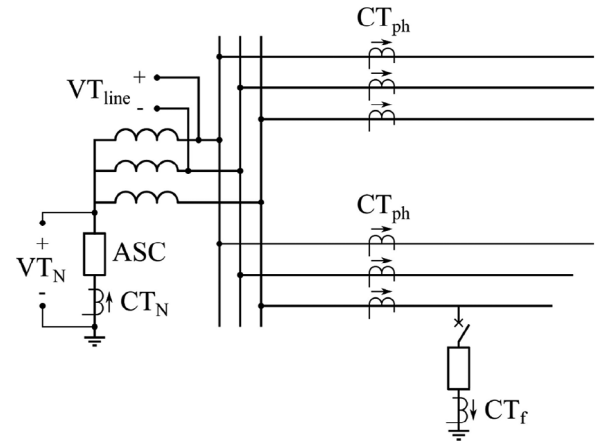| Current sensors	CT$_{ph}$ (default): Fluke i200s, set to 0.1V/A CT$_{ph,2}$: LEM HAS 50-s, 50/5A CT$_f$ and CT$_N$: Gossen Metrawatt WZ 12-C, 1mV/mA. Both I_f and I_n are measured on a 50-turn coil in order to better suit the measurement range of the probes used.
Voltage sensors	VT$_{line}$: Tektronix P5200, ratio 1V/500V VT$_N$: Tektronix P5200A, ratio 1V/50V
ASC	Leybold three-phase inductor, model nr. 732 42.
Other	Sampling frequency 4 kHz.

FIGURE 7   Test network single line diagram.
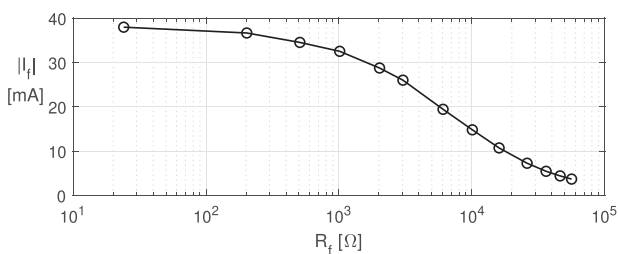
FIGURE 8   Measured fault current magnitude as function of fault resistance for the selected ASC setting.

FIGURE 9   Laboratory setup with equipment as given in Table 1.

shows the network topology, where two feeders with three PI-sections each can be operated radially or as a ring-network. The Pi-equivalents can be tuned to represent a 22 kV system with two radials with up to 24 km of overhead lines each, and the network has a voltage scaling of 22:0.4 and current scaling of 50:3 [25]. The network is supplied through a Δ/Y 400 V transformer which is grounded through an inductor for the tests considered in this paper.

4.1.2 | Network configuration

Both feeders represent 24 km of FeAl 240 mm^2 conductors. The laboratory network has a total of $3C_g$=2.4 μ F capacitance to ground, resulting in an uncompensated earth fault current of approximately 175 mA.

A variable inductor is placed in the transformer neutral to make the network resonant grounded. As the ASC is not perfectly linear, its impedance will vary with the voltage across it. This impedance is therefore estimated continuously by measuring the current and voltage of the ASC. Two resistor banks are used to provide loads up to 9 A and 3 A at the end of feeder 1 and 2, respectively. According to the laboratory documentation, this corresponds to loads in the range 50–150 A [25]. Finally, a variable resistor is connected between phase and ground through a controllable switch to emulate a high impedance fault. Figure 8 shows the magnitude of the fault current as function of the fault resistance obtained through measurements in the

lab with the chosen ASC setting. The complete setup of the lab and the equipment used is given in Table 1 and Figure 9, and an overview of the complete laboratory can be found in [25].

4.2 | Processing of measurements

4.2.1 | Phasor estimation

The fault detection method is based on current and voltage phasors. Most phasor estimation techniques assume a 50 Hz signal, and off-nominal frequencies result in a gradual drift of the phase angle over time. For many applications this is not an issue as the relationship between the phasors at any point in time is correct, but because the method presented in this paper relies on phasor increments, that is, changes over time, the phasor estimation must account for the drift in phase angle that can occur when the system frequency deviates from its nominal value.

The SDFT algorithm [26] is used for this purpose. It is based on a conventional recursive DFT-based phasor estimation, along with a frequency estimation stage. The frequency of the signal in each window is estimated based on the previous three consecutive phasor outputs using equations (10), (12) and (13) in [26]. By estimating the frequency of the signal at each sample, the expected drift in phase angle can be estimated. The resulting phasors can then be rotated back to their correct values, thus producing phasors with constant phase angles.

In order to produce a stable and accurate frequency estimate, a constant sinusoidal signal must be used. The line voltage is proposed to be used for this purpose as it remains constant during earth faults. The estimated phase angle drift based on this
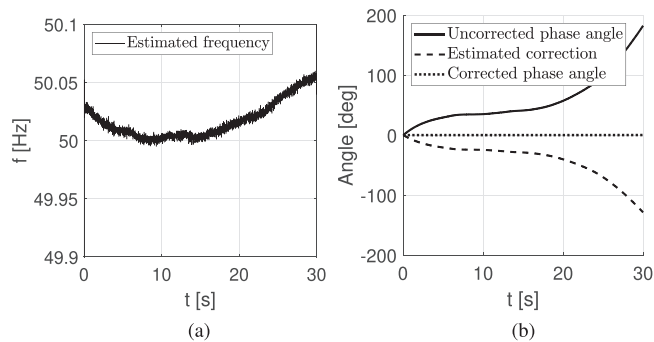
FIGURE 10 From measurement of the line voltage in the laboratory: (a) estimated frequency and (b) resulting phase angle with (dotted) and without (solid) correction of the phase angle drift.

voltage measurement is then used to correct all the other phasor estimates. A 100 Hz low-pass filter is applied to the line voltage measurements to give a better phasor estimation, whereas all other measurements are unfiltered.

Figure 10 shows the estimated frequency and resulting phasor angle before and after this method has been used. The uncorrected phasor angle which assumes a constant 50 Hz frequency can be seen to drift considerably.

5 | LABORATORY TEST RESULTS AND ANALYSIS

5.1 | Phase current indicators

To illustrate the desired response of the phase current indicators in (15), the faulty feeder indicators during a 5 kΩ fault is showed in Figure 11. It can be seen that the expected relationship between the three indicators is observed, both in terms of phase angles and magnitudes. Furthermore, the indicators relate to the fault current as predicted by (16). The fault detection response for phase a with settings ϵ_J=10 mA, T_{SW}=100 ms, K=0.1 and ϕ=15° is also shown on the right y-axis, illustrating that the fault detection logic is triggered both when the fault occurs as well as when it disappears. The indicators on the healthy feeder did not increase during the fault.

By inspection of Figure 11a, it can be seen that the phase current indicator magnitudes are not truly zero in healthy operation. These small fluctuations give rise to the need for the threshold ϵ_J to avoid frequent false detections in healthy operation, and this effectively limits the maximum sensitivity of the fault detection. Figure 12 shows the indicator magnitudes during a 20 kΩ fault, where the magnitude of the fault current and indicators no longer are detectable with the ϵ_J=10 mA setting. Furthermore, the magnitude of the fluctuations are now more significant compared to the fault current magnitude, distorting the ideal expected relationship between the three vectors as predicted by (16). Lowering the sensitivity threshold ϵ_J is thus not necessarily going to guarantee detection of very small fault currents, and it also increases the probability of false detections.
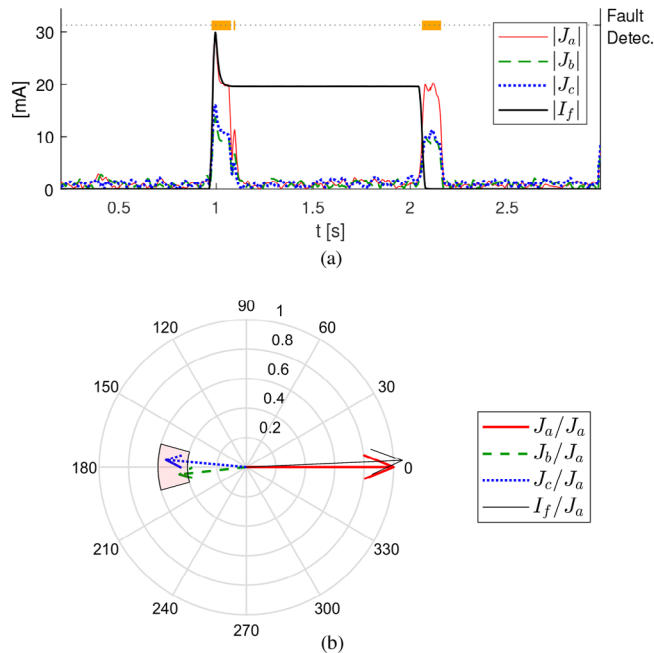

FIGURE 11 (a) Fault current and indicator magnitudes on the faulty feeder during a 5 kΩ fault, and (b) corresponding normalized vectors obtained at time t=1.02 s. The fault is applied at t=1 s and disconnected at t=2.1 s.
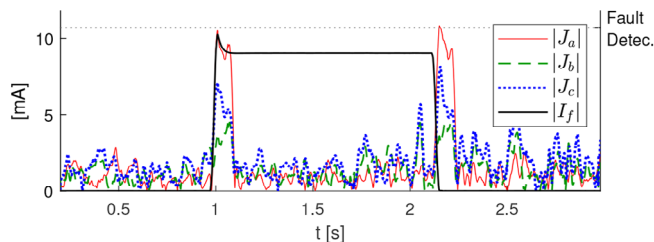

FIGURE 12 Indicator magnitudes during a 20 kΩ fault. The fault is applied at t=1 s and disconnected at t=2.2 s.

The indicators detected faults successfully up to 15 kΩ using ϵ_J = 10 mA.

To investigate the magnitude of the fluctuations, a constant load current was measured in the lab using two different sensors, that is, CT_{ph} and $CT_{ph,2}$ in Table 1. The resulting magnitude of the indicator J_a, computed with T_{SW}=100 ms, is shown in Figure 13. The different curves correspond to different nominal values of the load current, and the results illustrate clearly that the two sensors have different properties. In the case of $CT_{ph,2}$ sensor, the magnitudes are relatively large compared to CT_{ph}, but they are also independent of the magnitude of the primary current. CT_{ph} generally gives smaller fluctuations in J_a, but it is in turn dependent on the primary side current. Table 2 shows the number of false detections over the same period using CT_{ph}, as function of the load level and the sensitivity ϵ_J. To avoid false detection in this case the sensitivity must either (1) be limited to ϵ_J = 10 mA, or (2) adapted in real-time based on the present value of the load current, which would allow more sensitive settings during low-load conditions. To identify
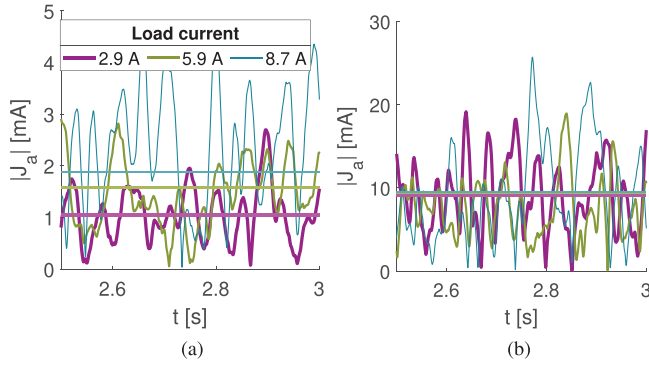
FIGURE 13 Magnitude of indicator J_a when measuring a constant load current with (a) the Fluke sensor or (b) the LEM sensor. Horizontal lines show average values over 30 s.

TABLE 2 Number of false detections during 30 s as function of load current $\vec{I}_L$, with $\phi = 15°$, $K = 0.1$, $T_{SW} = 0.1$ s.

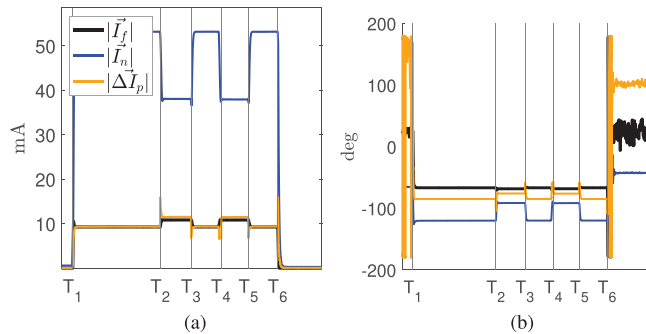| $\vec{I}_L$ [A]	$\epsilon_J = 4$ mA	$\epsilon_J = 6$ mA	$\epsilon_J = 8$ mA	$\epsilon_J = 10$ mA
2.9	2	0	0	0
5.9	22	1	1	0
8.7	35	3	0	0

FIGURE 14 Magnitude (a) and angle (b) of fault current, neutral current and $\Delta\vec{I}_p$ during sectionalizing process for a 20 kΩ fault.

the exact mechanism involved in determining the magnitude of these fluctuation requires further studies, but the importance of sensor quality is clearly seen.

5.2 | Sectionalizing

In order to verify the sectionalizing principle, a series of breaker operations is performed. By monitoring $\Delta\vec{I}_p$ throughout this process, the faulty section can be determined as explained in Section 3.3. Figure 14 illustrates how $\Delta\vec{I}_p$ is estimated throughout the sectionalizing sequence when clearing a fault, compared to both the fault current and the neutral current. The fault resistance was 20 kΩ. See Figure 7 for breaker locations:

- At $t = T_1$, the fault is applied between section 11 and L_{12}.

- At $t = T_2$, L_{13} is opened. Section 13 is now disconnected from the network, but the fault is still present. Disconnecting section 13 increased the compensation degree and decreased the neutral voltage. As a result, the neutral current decreased as well, but the fault current increased slightly. $\Delta\vec{I}_p$ correctly captures this behavior.
- At $t = T_3$, L_R is closed to bring section 13 back in, but now fed from feeder 2. The network now regains its original compensation degree.
- From $t = T_4$–T_5, section 12 is also disconnected from feeder 1 and connected to feeder 2.
- At $t = T_6$, the faulty section, section 11, is correctly disconnected by opening breaker L_{11}. $\Delta\vec{I}_p$ goes to zero, confirming that the fault is cleared.

The entire process from T_1 to T_6 took 11 s. Note that this breaker sequence is only intended to demonstrate the behavior of $\Delta\vec{I}_p$ during temporary disconnection of both healthy and faulty sections of the network. In a real network with a different feeder layout and breaker arrangement, the optimal breaker sequence may be different. The optimization of this sectionalizing process is not considered in this paper.

In addition to the case shown in Figure 14, the sectionalizing indicator was verified for faults in the range 10–50 kΩ. There were no signs of reduced accuracy for increased fault resistances, but fault resistances above 50 kΩ were not available at the time of testing. The indicator also functioned as intended in both an over-compensated and under-compensated network.

The network in the lab is very symmetrical, meaning that $\vec{V}_n$ and $\vec{I}_n$ are both very small in normal operation. This makes it quite easy to determine the presence of the fault based on either $\vec{V}_n$ or $\vec{I}_n$ as well, but in a network with a larger healthy state $\vec{V}_n$ and $\vec{I}_n$, this would not be possible. $\Delta\vec{I}_p$ could then provide a much more sensitive fault indication, because the change in compensation degree is accounted for. Furthermore, $\Delta\vec{I}_p$ will also match the faulty phase indicator J_a, enabling a more trustworthy and selective fault detection. The test shown in Figure 14 illustrates that $\Delta\vec{I}_p$ is a good approximation of the fault current, and it enables continuous monitoring of much higher fault resistances than $|V_n|$ can.

6 | LABORATORY VS. REAL NETWORKS

The results in Section 5 have verified the feasibility of the proposed method both for detecting and locating faults, and a few key factors have been identified and discussed in detail. It remains a challenge, however, to determine to what extent these laboratory tests can be used to predict the behavior in a real network.

6.1 | Scaling up the laboratory quantities

The first issue is the scaling of the laboratory model, and how the normal phase current indicator fluctuations (noise) are
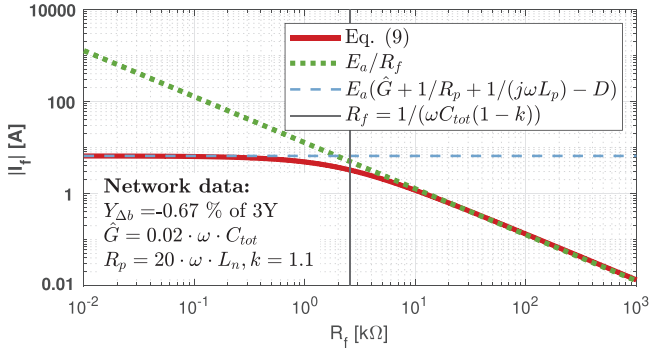
FIGURE 15 $|\vec{I}_f|$ computed using (9) and two approximations for low and high values of R_f, in a 22 kV network with a 50 A charging current.

FIGURE 16 Earth fault indicator magnitudes during a field test and laboratory test (right y-axis). R_f=20 kΩ in both cases, with pre-fault phase currents approximately 3 A and 20 A in the lab and the real network, respectively.

related to the load currents and the earth fault current. The results so far have shown that the phase current indicators are ultimately limited by the magnitudes of these fluctuations, as the fault current eventually fails to stand out above them when the fault resistance increases. The question then becomes how the currents and fault resistances should be scaled.

To analyse the sensitivity of the method, the system currents can be scaled based on the fault current's relationship with the network voltage. By analysing (9), it can be found that the fault current, for a given fault resistance, is proportional to the system voltage when the fault resistance is high enough. Exactly how high R_f needs to be for this approximation to be valid is best illustrated with a figure. Consider a hypothetical 22 kV network with a 50 A charging current $I_{ch} = \omega C_{tot} V_{LL}/\sqrt{3}$. The fault current magnitude is computed using (9) and two approximations of (9) valid at low and high fault resistances, respectively, as shown in Figure 15. The breaking point of the curve, marked by the vertical line, is found where $R_f^* = 1/(\omega C_{tot}(|1 - k|))$. This limit is approximately 10 kΩ in the lab, and it is lower in larger networks where C_{tot} is higher. Below this limit, the fault current is determined by multiple parameters such as $\hat{G}$, R_p, k and D, while the approximation $|\vec{I}_f| \approx |\vec{E}_a|/R_f$ is valid beyond R_f^*. The latter is therefore valid when discussing the upper limit of the method's sensitivity.

The above approximation implies that a fault resistance in the 400 V laboratory network is equivalent to a fault resistance 55 times higher in a 22 kV network (22/0.4 = 55). Alternatively, the fault current is increased 55 times when considering the same fault resistance in a 400 V and a 22 kV network. The laboratory load currents, which are in the range 2.9–8.7 A, will then correspond to 160–480 A in a 22 kV network. Similarly, the 175 mA capacitive charging current in the laboratory network will correspond to a 10 A current. 10 A is a too low value for a realistic resonant grounded network (a more realistic value would be in the range of 50 A and higher), but this will only impact $|\vec{I}_f|$ up to the threshold R_f^*. The unusually small charging current is therefore not affecting the fault current magnitude for high fault resistances, that is, at the maximum detectable fault resistance.

It is the method's maximum detectable fault resistance which is of primary interest to be able to scale so that it can be compared to other methods. The method proposed in this paper
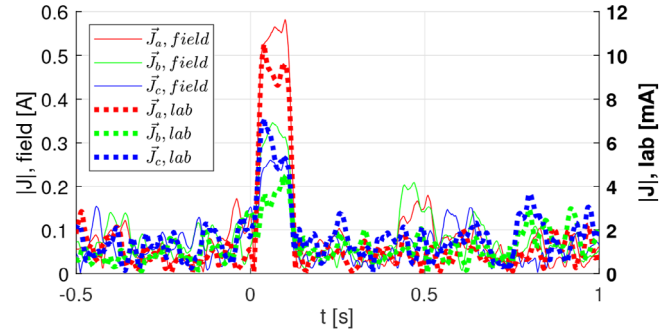
relies on detecting the fault current, and if the method's sensitivity is absolute—that is, it has some constant downward threshold for a detectable fault current—then the previous analysis have demonstrated that the laboratory results can be scaled directly based on the network voltage. This implies that a 20 kΩ fault resistance in the lab is equivalent to a 1.1 MΩ in the 22 kV network, which is not realistic. It is instead more reasonable to expect that the lowest detectable fault current will increase when moving from the 400 V laboratory to a 22 kV network, due to for instance increased measurement noise. The results so far have shown that the phase current fluctuations are the limiting factor, so the results in a real network will depend on how they scale. If their increase cancels out the effect of a larger fault current, then the maximum detectable fault resistance in the real network will be the same as in the laboratory. This remains uncertain until sensors and their properties can be studied in the field, as will be discussed next.

6.2 | Current sensor properties

The second challenge encountered when analysing these results is comparing the properties of the current sensors used in the laboratory to those of CTs in real networks. Figure 13 shows that two different sensors radically impacted the feasibility of the fault detection method. One of the sensors was impacted by the current magnitude, suggesting that the interference from surrounding conductors impacted its measurements. The other sensor, however, while being unaffected by the current magnitude, generally gave much higher measurement noise. Whether this is due to the measurement principle, current rating or something else entirely is not known. Whatever the reason, the results have shown that the indicators J_{a-c} will have a non-zero value in healthy operation, and a sufficiently large fault current is required to stand out above this noise.

Figure 16 shows the phase current indicator magnitudes on the faulty feeder measured during two 20 kΩ earth fault tests, where one set of measurements comes from the laboratory tests conducted in this paper, and the other from a field test conducted by Norwegian network operator Glitre Energi Nett in

their 22 kV network. The 22 kV network was operated with a 55 A ASC, which corresponded to a compensation degree of 10% over-compensation. Note that the indicators estimate a 10 mA and 0.55 A fault current in the two networks, fitting well with the analysis in Section 6.1 where a scaling factor of 55 was predicted. In the lab test the phase currents were 2.9 A, whereas they were 20 A in the field tests. Although the ratio between the fault current and the load currents is higher in the field tests, so is the ratio between the fluctuations and the load currents. In other words, the ratio between the fault current and the fluctuations is almost identical in the two recordings, making the fault detection equally challenging.

This finally raises the question about whether different sensors in the 22 kV network could have given better results and lower fluctuations. The field tests were conducted using class 5p20 protection cores, which are likely less accurate than the laboratory measurements. The field tests were not conducted with the purpose of verifying the method presented in this paper, and using metering cores or a different sensor type in a different location could have yielded different results. A detailed overview of the measurement chain used in the field tests is unfortunately not available, and their comparison with the lab tests is therefore done cautiously. The simple example in Figure 16 corroborates the lab results and demonstrates that the phase current indicators function as intended, but dedicated field tests are required to study the current sensors and the measurement quality in a real network, which currently is the limiting factor for the proposed method.

6.3 | Comparison with other methods

There are comparable methods found in the literature which are able to detect and locate faults for very high fault resistances, and which have been verified experimentally. These methods are all based on incremental values and on manipulating the same basic set of equations as in Section 2, but using zero-sequence currents. In [27], a probabilistic method is presented which functioned up to 220 kΩ, and the method in [3] can detect faults in the range 100–200 kΩ. The method in [28] functioned successfully up to 180 kΩ, but does require closed-ring operation of the network. Two methods functioning up to 100 kΩ are presented in [20], along with a fault location method aimed at narrowing down the faulted section. It is however dependent on detailed network data and may not always give a conclusive fault location estimate. The method in [19] functioned up to 160 kΩ, and the authors mention potential challenges with normal system operation triggering responses in the zero-sequence parameters similar to those observed during faults.

The sectionalizing indicator showed no considerable loss of accuracy up to the maximum available 50 kΩ fault resistance, indicating that its limit is well above 50 kΩ. The phase current indicators functioned up to 15–20 kΩ, but, as discussed earlier, the exact mechanism involved in determining this threshold is not fully understood. The scaling of the fault resistances in the lab is as discussed earlier a challenge; with ideal measurements the results can in theory be scaled up to any network by the same factor as the system voltage increase, but this implies sensitivity

in the MΩ-range for the proposed method and does not seem realistic. The evaluation of the fault resistances and their scaling can not be done separately from the analysis of the current sensors and their properties, and this does require field tests with applicable sensors.

Regarding the sectionalizing indicator, no comparable method for during-fault sectionalizing has been found in the literature.

7 | CONCLUSION

This paper has presented a detailed description of the implementation and laboratory verification of a novel earth fault detection and location method. The method shows promising results in the laboratory tests, and one field test from a 22 kV network corroborate this. The main contributions of these results are as follows:

1) The new method makes each feeder capable of determining a forward fault using only local phase current measurements without need for input from other feeders or using voltage as a polarizing quantity.
2) A sectionalizing indicator is presented and verified, which can be used to provide continuous fault indication in a network during the sectionalizing process. The indicator is based on the neutral current in the network and is not limited to radial networks.

The results also show that phase currents can be used for low-current earth faults, a domain which traditionally has been handled exclusively with zero-sequence currents.

In addition to the mentioned contributions, the paper has also identified limitations, both of the method itself and the applicability of the tests, as well as further work required before the method can be implemented. The measurement quality is currently identified as the main limitation of the method, and 50 Hz noise found to be dependent on the current sensors and the magnitude of the load currents limits the sensitivity. This phenomenon is dependent on the sensors used, and understanding and quantifying this represents the most important future work as it relates directly to the attainable sensitivity and reliable pickup levels for the fault detection. Dedicated field tests are required to study the impact of different current sensors and CT cores on the method further.

CONFLICT OF INTEREST STATEMENT

The authors have declared no conflict of interest.

DATA AVAILABILITY STATEMENT

Research data are not shared.

ORCID

Thomas Treider https://orcid.org/0000-0001-9858-5032

REFERENCES

1. Norwegian Directorate for Civil Protection (DSB). Veiledning til forskrift om elektriske forsyningsanlegg (In Norwegian). dsb.no. https://www.dsb.no/lover/elektriske-anlegg-og-elektrisk-utstyr/veiledning-til-forskrift/veiledning-til-forskrift-om-elektriske-forsyningsanlegg/. Accessed 25 June 2023
2. Hänninen, S., Lehtonen, M.: Characteristics of earth faults in electrical distribution networks with high impedance earthing. Electr. Power Syst. Res. 44(3), 155–161 (1998)
3. Nikander, A., Järventausta, P.: Identification of high-impedance earth faults in neutral isolated or compensated MV Nntworks. IEEE Trans. Power Delivery 32(3), 1187–1195 (2017). doi: https://doi.org/10.1109/TPWRD.2014.2346831
4. Wang, X., Wei, X., Gao, J., Song, G., Kheshti, M., Guo, L.: High-impedance fault detection method based on stochastic resonance for a Distribution Network With Strong Background Noise. IEEE Trans. Power Delivery 37(2), 1004–1016 (2022). doi: https://doi.org/10.1109/TPWRD.2021.3075472
5. Schinerl, T.: A new sensitive detection algorithm for low and high impedance earth faults in compensated MV networks based on the admittance method. CIRED 2005-18th International Conference and Exhibition on Electricity Distribution, pp. 1–4. IEEE, Piscataway (2005). doi: https://doi.org/10.1049/cp:20051166
6. Altonen, J., Wahlroos, A., Vähäkuopus, S.: Application of multi-frequency admittance-based fault passage indication in practical compensated medium-voltage network. CIRED-Open Access Proc. J. 2017(1), 947–951 (2017). doi: https://doi.org/10.1049/oap-cired.2017.0967
7. Druml, G., Raunig, C., Schegner, P., Fickert, L.: Fast selective earth fault localization using the new fast pulse detection method. In: 22nd International Conference and Exhibition on Electricity Distribution (CIRED 2013), pp. 1–5. IEEE, Piscataway (2013)
8. Farughian, A., Kumpulainen, L., Kauhaniemi, K.: Review of methodologies for earth fault indication and location in compensated and unearthed MV distribution networks. Electr. Power Syst. Res. 154, 373–380 (2018)
9. Wang, P., Chen, B., Zhou, H., Cuihua, T., Sun, B.: Fault Location in Resonant Grounded Network by Adaptive Control of Neutral-to-Earth Complex Impedance. IEEE Trans. Power Delivery 33(2), 689–698 (2018). doi: https://doi.org/10.1109/TPWRD.2017.2716955
10. Burkhardt, E., Fickert, L., Jenau, F.: The "short-term compensation change" to detect earth faults in compensated networks. In: 2020 55th International Universities Power Engineering Conference (UPEC), pp. 1–5. IEEE, Piscataway (2020). doi: https://doi.org/10.1109/UPEC49904.2020.9209841
11. Raunig, C., Fickert, L., Obkircher, C., Achleitner, G.: Mobile earth fault localization by tracing current injection. In: Proceedings of the 2010 Electric Power Quality and Supply Reliability Conference, pp. 243–246. IEEE, Piscataway (2010). doi: https://doi.org/10.1109/PQ.2010.5549991
12. Li, J., Liu, Y., Li, C., Zeng, D., Li, H., Wang, G.: An FTU-based method for locating single-phase high-impedance faults using transient zero-sequence admittance in resonant grounding systems. IEEE Trans. Power Delivery 37(2), 913–922 (2022). doi: https://doi.org/10.1109/TPWRD.2021.3074217
13. Loos, M., Werben, S., Kereit, M., Maun, J.: Fault direction method in compensated network using the zero sequence active energy signal. Eurocon 2013, 717–723 (2013). doi: https://doi.org/10.1109/EUROCON.2013.6625062
14. Ji, H., Yang, Y., Lian, H., Cong, S.: Effect on earth fault detection based on energy function caused by imbalance of three-phase earth capacitance in resonant grounded system. In: 2006 International Conference on Power System Technology, pp. 1–5. IEEE, Piscataway (2006). doi: https://doi.org/10.1109/ICPST.2006.321670
15. Pandakov, K., Høidalen, H.K., Marvik, J.I.: Misoperation analysis of steady-state and transient methods on earth fault locating in compensated distribution networks. Sustain. Energy Grids Netw. 15, 34–42 (2018). https://doi.org/10.1016/j.segan.2017.12.001
16. Pirmani, S.K., Mahmud, Md. A., Islam, S.N., Arif, M.T.: A modified charge similarity approach for detecting high impedance earth faults in resonant grounded power distribution networks. Electr. Power Syst. Res. 220, 109264 (2023)
17. Pandakov, K.: Improvements in protection of medium voltage resonant grounded networks with distributed sources. Ph.D. Dissertation, Department of Electric Power Engineering, NTNU, Trondheim, Norway (2018)
18. Barik, M.A., Gargoom, A., Mahmud, M.A., Haque, M.E., Al-Khalidi, H., Than Oo, A.M.: A decentralized fault detection technique for detecting single phase to ground faults in power distribution systems with resonant grounding. IEEE Trans. Power Delivery 33(5), 2462–2473 (2018). doi: https://doi.org/10.1109/TPWRD.2018.2799181
19. Hänninen, S., Lehtonen, M.: Method for detection and location of very high resistive earth faults. ETEP 9(5), 285–291 (1999)
20. Welfonder, T., Leitloff, V., Fenillet, R., Vitet, S.: Location strategies and evaluation of detection algorithms for earth faults in compensated MV distribution systems. IEEE Trans. Power Delivery 15(4), 1121–1128 (2000). doi: https://doi.org/10.1109/61.891492
21. Sagastabeitia, K.J., Zamora, I., Mazónm, A.J., Agiako, Z., Buigues, G.: Low-current fault detection in high impedance grounded distribution networks, using residual variations of asymmetries. IET Gener. Transm. Distrib. 6(12), 1252–1261 (2012)
22. Treider, T., Gustavsen, B., Høidalen, H.K.: Steady-state, iterative method for locating and clearing permanent high impedance earth faults in compensated networks. In: 16th International Conference on Developments in Power System Protection 2022 (DPSP 2022), pp. 1–6. IET, Stevenage (2022)
23. Norwegian University of Science and Technology. National Smart Grid Laboratory. https://www.ntnu.edu/smartgrid. Accessed 25 June 2023
24. SINTEF. Smart Grid Laboratory. https://www.sintef.no/en/all-laboratories/smartgridlaboratory/. Accessed 25 June 2023
25. Petterteig, A.: Distribution Network Laboratory Model: Consisting of a HV/MV substation model, a synchronous generator DG model and a flexible line equivalent. Rep. TR A7122, SINTEF Energy Research, Trondheim, Norway (2011)
26. Gurusinghe, D.R., Ouellette, D., Rajapakse, A.D.: Implementation of smart DFT-based PMU model in the real-rime digital simulator. Paper presented at international conference on power systems transients (IPST2017), pp. 1–6, Seoul, Republic of Korea, 26–29 June 2017
27. Hänninen, S., Lehtonen, M., Pulkkinen, U.: A probabilistic method for detection and location of very high resistive earth faults. Electr. Power Syst. Res. 54(3), 199–206 (2000)
28. Nikander, A., Repo, S., Järventausta, P.: Utilizing the ring operation mode of medium voltage distribution feeders. In: 17th International Conference and Exhibition on Electricity Distribution (CIRED 2003), pp. 1–6. IET, Stevenage (2003)